Chapter 3

Experimental Methods and Data Reduction

3.1 Overview

Two main types of measurement were performed in the study of these turbulent flow fields. Velocity measurements were performed using a 2-D Laser Doppler Velocimeter (LDV). The second type of measurement used consists of acoustic measurements. Acoustic measurements serve to support the velocity measurements especially in the study of the flow dynamics described in Chapter 5. Design, operation and maintenance of the LDV is described in detail in Appendix A. The pressure sensor design and calibration is described in detail in Appendix B.

3.2 Velocity measurements

Velocity measurements using a LDV are often used for highly separated flows because the measurement is non-intrusive and when properly set up the LDV is capable of measuring both positive and negative velocities. Statistical moment calculations and frequency domain calculations are however much more involved due to the fact that the data points are non-uniformly spaced in time. For an ideal LDV, the time between data points is random, with a Poisson distribution.

3.2.1 LDV overview

Although LDV design is described in detail in Appendix A it is worthwhile here to briefly give an overview of some interesting aspects of the present implementation.

The laser used is a 5W Argon-Ion laser operating in multi-band mode so that a range of visible Argon laser lines are excited. The most dominant among these wavelengths are: 514.5 nm, 496 nm, 488 nm and 476 nm. The two most powerful lines are the 514.5 nm (green) and 488 nm (blue) laser lines. These two lines are used for the 2-D LDV.

The LDV measures velocity by collecting scattered light from the diffraction pattern formed when two coherent laser beams are focused to the same location in space. The scattered light is modulated at a frequency proportional to the scattering

particle's velocity. Additionally, one of the two beams may be frequency shifted to generate a moving diffraction pattern which then allows not only velocity magnitude but also direction to be determined. A 2-D LDV uses two pairs of laser beams focused to the same spot. Each beam pair measures a velocity vector. If both beam pairs are focused using the same lens, as is the case here, then the two measured velocity vectors lie in the same plane.

In the present setup, a green beam pair and blue beam pair are focused using a single 4" achromatic lens. One beam of each pair is frequency shifted by 40 MHz. The fringe spacing can be calculated to be $1.71\mu m$ and $1.62\mu m$ for the green and blue diffraction pattern, respectively. The green (blue) ellipsoidal measurement volume measures 0.49 mm (0.47 mm) on the major axis and 0.075 mm (0.071 mm) on the minor axis. Each beam pair is coupled into a single optical fiber to prevent different fiber lengths or material strains from affecting beam coherence at the measurement volume.

The scattered light is collected by a 2" achromatic lens, focusing the light into a $50\mu m$ core multi–mode fiber optic cable. Upon exit from the multimode fiber, the light is collimated and separated by wavelength using a dichroic mirror. The separated beams are then further narrow bandpass filtered for the respective wavelengths (488 nm and 514.5 nm).

The filtered light flux is converted to electric current by a photo multiplier tube (PMT). The output of the PMT is transimpedance amplified and then high pass filtered (25 MHz cut-off frequency). The electronic signal is then mixed with a reference frequency. The output of the mixer is low pass filtered (cut-off frequency of 30 MHz) to isolate the frequency difference component of the mixer output. The output of the low pass filter is amplified using a custom built high bandwidth op-amp circuit and then sent on for collection by high speed data acquisition. The output from the op-amp circuit is also used as the input to a trigger circuit that is used to determine the presence of a Doppler burst in the electronic signal. The issued trigger is used to initiate the high speed A/D Doppler burst collection and to time stamp the occurrence of the burst. The system supports three trigger sources. The system can trigger on the

presence of a green or blue burst alone, or it can trigger only if both a green and blue burst are detected within a given coincidence window. For any trigger mode however, when a trigger is issued both the green and blue electronic signals are collected. Thus the system always takes coincident data. The system can take successive bursts until the onboard memory of the high speed data acquisition card has been filled. For lower flow velocities, where a 25 MHz burst sampling frequency was sufficient, 256 samples are collected for each burst and 8065 bursts can be collected for each velocity component. For higher flow velocities, the burst length had to be increased to 512 samples to maintain frequency estimation accuracy and consequently only 4064 bursts could be collected for each of the velocity components. To obtain sufficient data to form reliable statistical quantities and reasonably smooth power spectra, multiple blocks of 4064 or 8065 bursts were collected. Ideally, based on the memory on the board, 4096 and 8192 bursts should be able to be collected respectively. However, the high speed data acquisition board uses some of the memory to store the memory address of the exact starting and stopping points of each burst.

The collected bursts are analyzed for frequency content using an autoregressive scheme with 20 parameters representing the spectrum (Marple, 1987). The spectrum peak is found by quadratic interpolation of the logarithmic power spectrum values. In addition to the frequency, a measure of the signal to noise ratio (SNR) is also calculated. For the present application the SNR is defined as the logarithm of the peak interpolated power spectrum magnitude divided by the average power spectrum value. The calculated SNR is used to discard low quality Doppler bursts from the data set. Generally, data points with an SNR greater than 1.50 were found to be acceptable.

The trigger pulse widths of both trigger circuits can be adjusted using potentiometer dials. The data acquisition trigger pulse width can also be changed by potentiometer. The data acquisition trigger pulse width can be used to inhibit the LDV from data collection for some short period of time. For the measurements presented herein the maximum repeat frequency was allowed to be around 20,000 Hz. For this high trigger rate, it is likely that a given particles' velocity was measured

more than once while in the measurement volume. Investigations using sinusoidal excitation showed that the high trigger repeat frequency does not affect the results adversely. Even at a frequency of 400 Hz, the sinusoidal velocity response was unaffected. Inhibition of the trigger is important in cases where large seed particles that are unable to follow the flow adequately are present and could cause errors in the measurement. The present LDV is virtually immune to such a situation because particles too large to follow the flow adequately are also too large to generate well defined Doppler bursts due to the relatively small fringe spacing.

3.2.2 Velocity statistics

The interpretation of time resolved velocity data from LDV measurements received a lot of attention early in the evolution of the instrument (Donohue et al., 1972). The major concern is that the random sample rate introduces a bias in the statistics calculated from an ensemble of data points (i.e. statistics weighted on a point by point basis). The bias stems from the fact that if seed particles are uniformly distributed in the flow to be measured, then more Doppler bursts will be registered during a period of high velocity than during a period of low velocity. Consequently, different algorithms have been developed to remove such a bias from the calculated statistics. The most popular among these are the residence time weighted statistics and the inter–arrival time weighted statistics methods. The residence time weighted statistics are computed from a knowledge of a given bursts' actual length. The longer a burst lasts, the higher its weight. Some LDV burst processors are especially well equipped to measure the burst length as it is essentially a byproduct of the burst frequency calculation. The inter–arrival time weighted statistics method is nothing more than a discrete integral form of the original time average definition, i.e. signal integrated over a period time T divided by the period. This form of the velocity statistics calculation is used here. The calculation for the mean of a quantity and its standard deviation are given in both the time continuous and discrete forms in Equations 3.1 and 3.2 respectively. The standard deviation can also be called the Root Mean Square (RMS) value of a data set and the discussion from here on will use

the term RMS instead of standard deviation to refer to the first moment of a data set about its mean.

$$\bar{q} = \int_0^T q dt \approx \sum_{j=2}^{N-1} \left(q_j \frac{t_{j+1} - t_{j-1}}{2} \right) + q_1 \frac{t_2 - t_1}{2} + q_N \frac{t_N - t_{N-1}}{2} \tag{3.1}$$

$$q_{rms} = \int_0^T (q - \bar{q})^2 dt \approx \sum_{j=2}^{N-1} \left((q_j - \bar{q})^2 \frac{t_{j+1} - t_{j-1}}{2} \right) + (q_1 - \bar{q})^2 \frac{t_2 - t_1}{2} + (q_N - \bar{q})^2 \frac{t_N - t_{N-1}}{2} \tag{3.2}$$

The Reynolds stresses are an important quantity in the description of turbulent flows. In total, there are nine Reynolds stresses of which six are independent. Three of the stresses, the normal stresses are simply equal to the variance of the three independent velocity components. The variance is equal to the square of the RMS value. The other three stresses are the time average of the product of two different velocity components' fluctuating parts. In the present study using a 2-D LDV, only the $\overline{uw}$ component of these three stresses can be measured. The equation for the calculation of this stress is given in Equation 3.3. All together, three of the six Reynolds stresses are able to be measured using the present measurement setup: $\overline{uw}$, $\overline{uu}$, $\overline{ww}$.

$$\overline{uw} = \int_0^T \left((u - \bar{u}) * (w - \bar{w}) \right) dt \tag{3.3}$$

Another important device in the characterization of a velocity field is the histogram. The histogram of velocities often helps characterize the type of flow fluctuations present. The histogram is also helpful in evaluating the validity of a given data set by clearly revealing any significant data cut-off, if for example the mixing frequency used is too high. Histograms were calculated for all data sets taken in the present research effort. The histograms divide the collected data into 200 bins between the maximum and minimum in the given data set. The high number of bins

used allows a relatively smooth distribution to be calculated for most data points, except in cases where the distribution is very narrow. For very narrow distributions, the bin width begins to be on the order of the accuracy of the LDV resulting in a non-smooth distribution.

3.2.3 Flow characterization

As seen in Section 1.3 the two most important non-dimensional parameters characterizing a swirling flow field are the Reynolds number and swirl number. Reynolds numbers reported in the present study, unless specified as local, will use the area average nozzle velocity and nozzle size as characteristic length scales. For the case without center–body the nozzle size is equal to the diameter of the nozzle. For the case where the nozzle flow is annular due to the presence of a cylindrical center–body, the nozzle size is equal to its hydraulic diameter which is the difference between the nozzle diameter and the center–body diameter (White, 1994). The equation for the Reynolds number is given in Equation 3.4.

$$Re = \frac{U_{avg} N_{sz}}{\nu} \tag{3.4}$$

The swirl number has been defined a myriad of ways. Two definitions will be reported here. The first swirl number is based on the strict ratio of mean momentum fluxes, neglecting turbulence transport. This swirl number will be referred to as the laminar swirl number and is defined by Equation 3.5(e.g. Gouldin et al., 1985). The second swirl number accounts for turbulent transport in addition to the mean momentum fluxes. The second swirl number will be referred to as the turbulent swirl number and is defined by Equation 3.6 (e.g. Holzäpfel et al., 1996). In general the laminar and turbulent swirl numbers are very similar. If the two differ by more than one percent, both swirl numbers will be given.

$$\frac{\int_{R_1}^{R_2} \bar{U}\bar{W}r^2 dr}{R_2 \int_{R_1}^{R_2} \bar{U}^2 r dr} \tag{3.5}$$

$$\frac{2\pi \int_{R_1}^{R_2} \rho \left(\bar{U}\bar{W} + \overline{u'w'}\right) r^2 dr}{2\pi R_2 \int_{R_1}^{R_2} \rho \left(\bar{U}^2 + \overline{u'}^2\right) r dr} \tag{3.6}$$

3.2.4 Frequency domain

3.2.4.1 Introduction to power spectrum calculation methods

The transformation of the unevenly sampled data into the frequency domain is a very difficult subject that has been dealt with in different ways in different areas of science. In most cases researchers were concerned with obtaining correct estimates of the power spectrum or periodogram of the unevenly sampled data. The first approach used in fluid dynamics was introduced by Gaster and Roberts (1977). The calculation of the power spectrum consists of essentially a modified Direct Fourier Transform (DFT) method. The equation for the calculation is given in Equation 3.7. Two aspects of Equation 3.7 are important to note. The power spectrum is not weighted according to time interval but by point. In this manner, data points with a relatively large time interval do not contribute more to the power spectrum estimate than any other points. Additionally, Equation 3.7 subtracts an offset proportional to the variance of the data set from the direct DFT-like calculation. Gaster and Roberts (1977) showed that the offset can be calculated to have the precise form in Equation 3.7 if the inter arrival times of the bursts have a Poisson distribution. Furthermore, if the data is divided up into blocks and the estimates of the resulting blocks are averaged, the variance of the estimate can be significantly reduced (Roberts and Gaster, 1980). Roberts et al. (1980) demonstrate the effective use of the variance reducing scheme for real LDV data. The estimate derived from Equation 3.7 will be referred to as the Gaster estimate.

$$Psd(f) = \frac{2}{f_{sam} T} \left[\left| \sum_j q(t_j) e^{i2\pi f t_j} \right|^2 - \sum_j q^2(t_j) \right] \tag{3.7}$$

The second method for power spectrum calculation is presented in Press et al. (1992), stemming from the work of Lomb (1976) and Press and Rybicki (1989) in

astrophysics. In this area of science, the possible periodicity of non-continuous events is often the subject of investigation. The equation for the normalized power spectrum is shown in Equation 3.8. The equation can be evaluated at any frequency, although for a given data set, only a certain set of frequency data points of the periodogram are independent. These points can not be calculated and a periodogram calculated by Equation 3.8 must be interpreted as an at least in part interpolated power spectrum. It can be shown that the algorithm of Equation 3.8 reduces to the calculation of a best fit approximation to the data using sines and cosines of the frequency in question. For historical reasons outlined in Press et al. (1992), the estimate given by Equation 3.8 will be referred to as the Lomb estimate.

$$\tan 2\omega\tau = \frac{\sum_j (\sin 2\omega t_j)}{\sum_j (\cos 2\omega t_j)}$$

$$Ps(f) = \frac{1}{2q_{rms}^2} \left\{ \frac{\left[\sum_j ((q_j - \bar{q}) \cos \omega(t_j - \tau))\right]^2}{\sum_j \cos^2 \omega(t_j - \tau)} + \frac{\left[\sum_j ((q_j - \bar{q}) \sin \omega(t_j - \tau))\right]^2}{\sum_j \sin^2 \omega(t_j - \tau)} \right\} \tag{3.8}$$

It must be added that no matter how the estimate for the power spectrum is calculated, the benefit of random sampling allows the calculated frequency range to be extended. For truly randomly sampled data, aliasing is not possible in the frequency interval all the way up to the mean sampling frequency. In practice, since the data sets have a limited length, valuable information beyond the established limit for uniform sampling can be obtained, but not up to the mean sampling frequency. The exact useful upper limit of evaluation is a function of the precise distribution of sampling intervals and cannot be calculated directly. The power spectra presented here are not calculated beyond 0.75 times the mean sampling frequency, a range justifiable given the work presented below.

Neither one of the two methods discussed sofar allows the transformation of the collected data into the frequency domain. One of the reasons for actual transformation into the frequency domain is that such a transformation would allow cross-spectra of velocity components and acoustic pressure to be calculated, along with transfer

functions among these quantities. Presentations of such results have sofar not been found in literature. The method used here to obtain an estimate of the frequency domain representation of the data is given in Equation 3.9 and goes directly back to the definition of the DFT. The integral's discrete data point form is also given in Equation 3.9. The power spectrum is calculated from the DFT using Equation 3.10. The power spectrum estimate using Equation 3.9 will be referred to as the DFT estimate. Expressions for the cross spectrum of two data sets, the transfer function estimate and the coherence are given in Equation 3.11 through 3.13 respectively.

$$DFT(f) = \frac{1}{T}\int_0^T q(t)e^{-i2\pi ft}dt \approx$$
$$\frac{1}{T}\left(\sum_{j=2}^{N-1} q_j\ e^{i2\pi f_k t_j}\frac{t_{j+1}-t_{j-1}}{2} + q_1\ e^{i2\pi f_k t_1}\frac{t_2-t_1}{2} + q_N\ e^{i2\pi f_k t_N}\frac{t_N-t_{N-1}}{2}\right) \tag{3.9}$$

$$Ps(f) = DFT(f)^* DFT(f) \tag{3.10}$$

$$CPs_{12}(f) = DFT_1(f)^* DFT_2(f) \tag{3.11}$$

$$TF_{12}(f) = \frac{CPs_{12}(f)}{Ps_1(f)} \tag{3.12}$$

$$COH_{12}(f) = \frac{|CPs_{12}|^2}{Ps_1(f)Ps_2(f)} \tag{3.13}$$

3.2.4.2 Comparison of presented methods for power spectrum calculation

In the following, the three methods outlined will be compared on a variety of trial data sets. The standard of comparison that will be used is the result from the analogous evenly spaced data set using normal FFT transformation to get into the frequency domain. The power spectrum estimate derived from the FFT calculation will be referred to as the FFT estimate. Both evenly spaced time data sets and Poisson distributed sample time data sets will be studied. Some actual LDV sample time distributions will also be tested. The probability density function for an ideal

Poisson distributed data set and for two types of actual LDV sample times are shown in Figure 3.1. The two types of LDV sample times correspond to the two extremes of LDV measurement environments: low and high turbulence. The low turbulence sample time distribution is taken from a data set taken inside the nozzle of the experimental rig. The turbulence level there is less than 10%. The high turbulence sample time distribution is taken from the edge of a recirculation zone where the RMS value is 3 m/sec and the mean velocity is essentially zero. The figure shows that there are no significant differences in the distribution of the sample times depending on turbulence intensity. Such an influence is predicted by the model of Tropea (1987).

It is possible that the sample time distribution would change for cases where the seed concentration is low. In the experiments reported herein, the seed level is relatively high and apparently turbulence is not causing a significant change in the sample time distribution. Both distributions are reasonably well approximated by the ideal Poisson distribution, except at the ends of the distribution. For long sample times, there simply aren't enough data points to be able to form a reliable approximation to the probability density function. At low sample times the deviation from the ideal distribution is likely caused by the fact that the LDV system is inhibited some finite amount of time after each burst, due to the trigger pulse width.

The analysis largely follows that of Tropea (1987). An autoregressive model of second order is used to generate a data series with a known power spectral density (PSD). In the present analysis, four data sets will be tested. The first is a first order spectrum, identical to that used by Tropea (1987). Additionally, a second order spectrum, a first order spectrum with white noise and a second order spectrum with two sine waves are studied. The generated data series is not restricted to a particular sample rate and can be scaled to any value with the proportional shift in the spectrum. To stay non-dimensional, the time interval was chosen as one for the autoregressive series. The spectrum generated contains energy up to a frequency of 0.5 (relative to the time step of 1). This means that all of the energy is represented by the data set with a time spacing of one.

The randomly sampled data is interpolated at some lower sampling rate from the

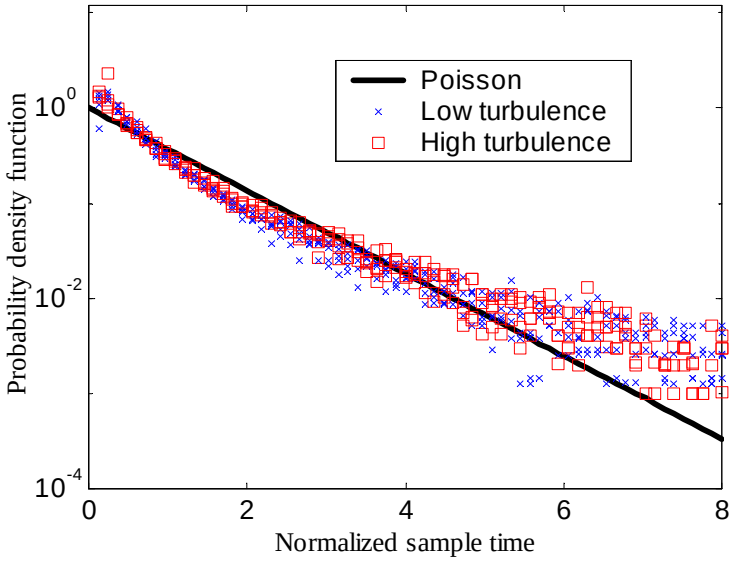

Figure 3.1: Ideal Poisson distribution compared to two typical LDV sample time distributions

primary evenly spaced data series. Spline interpolation is used to obtain the estimates between the regularly spaced intervals. Since the regularly spaced data set is complete from an information standpoint, it is expected that interpolation will not alter the spectral characteristics of the data in the frequency range of the primary signal. To support the claim that interpolation does not change the spectrum, a primary second order data series was generated and interpolated at twice its original frequency at times always between points in the primary data series. The FFT calculated PSDs of both time series and the true PSD are shown in Figure 3.2. There are no effects due to interpolation present in the data set at frequencies below 0.4, which is close to what was expected based on the information argument.

In order to study the estimation methods in a familiar environment, all the methods are applied to the evenly spaced primary data set (second order spectrum). The data set is divided into blocks of 512 samples and then averaged. The record is long enough to accommodate 256 averages. The results shown in Figure 3.3 demonstrate that all methods perform fairly well except the Gaster estimate. However, this is not surprising considering the estimate was specifically designed for Poisson distributed

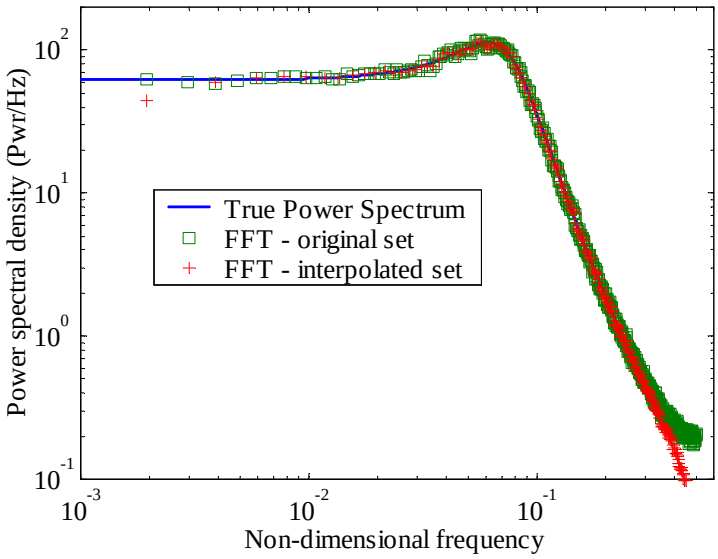

Figure 3.2: True second order PSD with the FFT calculated spectra of the primary data series and an interpolated data series

sample times. The effect of the subtracted offset can be clearly identified in the PSD estimate.

Figure 3.4 shows the results for Poisson distributed sample times around a mean frequency equal to that of the primary data series. Only 16 averages over blocks of length 512 are taken. The results show that the Gaster estimate follows the true spectrum most closely. The Lomb estimate exhibits an offset that doesn't become clear until a frequency of approximately 0.02. The DFT estimate matches the Gaster estimate to a frequency close to 0.08, but then drifts up and approaches the Lomb estimate. All estimates show the effects of a relatively large variance. Figure 3.5 shows the results for 256 averages. The quality of the estimates has not changed significantly, but the variance of all estimates appears clearly reduced.

Figure 3.6 shows the results for Poisson distributed sample times with a mean sampling rate 25% slower than the primary data series. The data set has a second order power spectrum and 256 averages using blocks of 512 samples were used to obtain the estimates. The results are very similar to Figure 3.5. The Gaster estimate

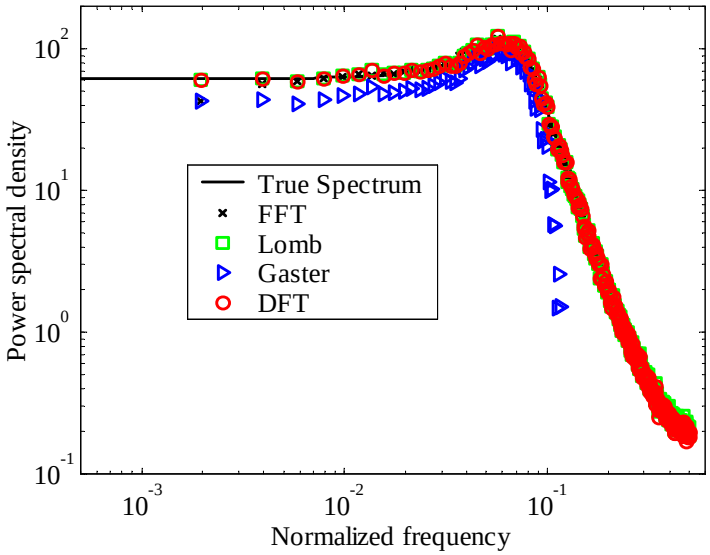

Figure 3.3: PSD estimates of a second order spectrum using the primary evenly spaced data series

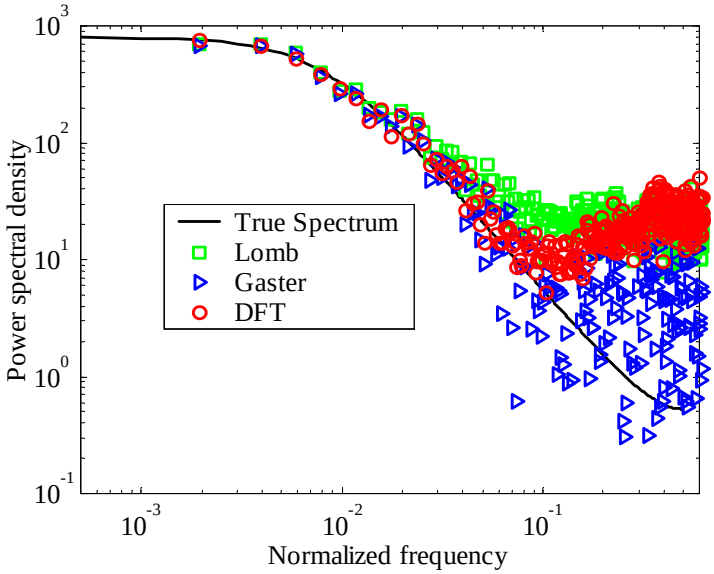

Figure 3.4: PSD estimates of a first order spectrum using Poisson distributed sample times (16 averages)

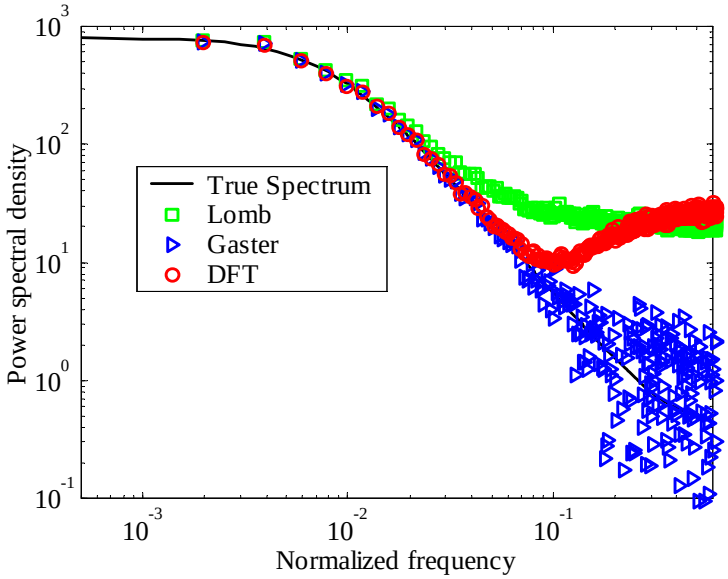

Figure 3.5: PSD estimates of a first order spectrum using Poisson distributed sample times (256 averages)

performs best followed by the DFT estimate and the Lomb estimate. The DFT estimate continues to exhibit very little offset until a frequency of about 0.08, whereas the offset for the Lomb estimate appears more constant. The variance in the Gaster estimate appears larger than for the other estimates, but this is due to the logarithmic scale used in the plot. Figure 3.7 shows the results under identical conditions, except that the sampling rate has been further reduced to 50% of the original primary data set. The results are very similar for the Gaster estimate. The Gaster estimate seems to be able to predict the spectrum over its entire range, except that the variance appears to have increased over the estimate shown in Figure 3.6. Indeed, Gaster and Roberts (1977) report that the variance in the estimate is inversely proportional to the sampling rate. It is not possible to draw strong conclusions concerning the matter of aliasing based on Figure 3.7 since very little energy is contained beyond the Nyquist frequency of 0.25. Note also that the block size used is relatively large at 512 samples. A smoother estimate using the same number of samples could be obtained by reducing the block length. The smoother estimates would be generated

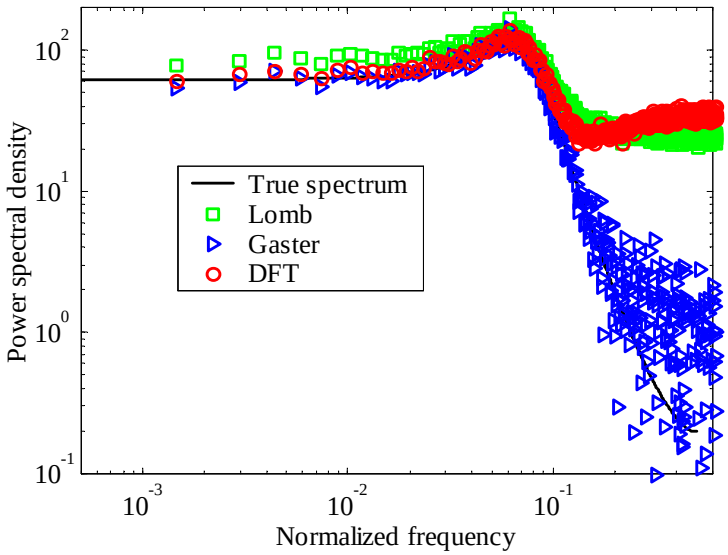

Figure 3.6: PSD estimates of a second order spectrum using Poisson distributed sample times (256 averages - mean frequency 75% of primary series)

at the expense of frequency resolution.

The matter of aliasing is addressed further in Figure 3.8 which shows the spectra of the same second order data set, except that two sine waves are added. The sine waves are of unity magnitude and located at frequencies of 0.02 and 0.375. The second of the sine waves is located outside the Nyquist interval since the mean sampling frequency for these estimates is 0.5. The energy in the second sine wave is clearly significant enough to generate aliased energy in the spectrum. The results however clearly show that that all estimators locate both sine waves and accurately represent their magnitude. None of the estimates show aliased energy below the Nyquist frequency of 0.25.

Figure 3.9 shows the results for a data set where white noise was added to the primary data series before interpolation. The sample frequency was increased back to 75% of the primary data series frequency. All estimates show the effect of the added noise. Once again, the Gaster estimate performs best. The tail-off at high frequency is due to the fact that the random data set was interpolated from the primary data

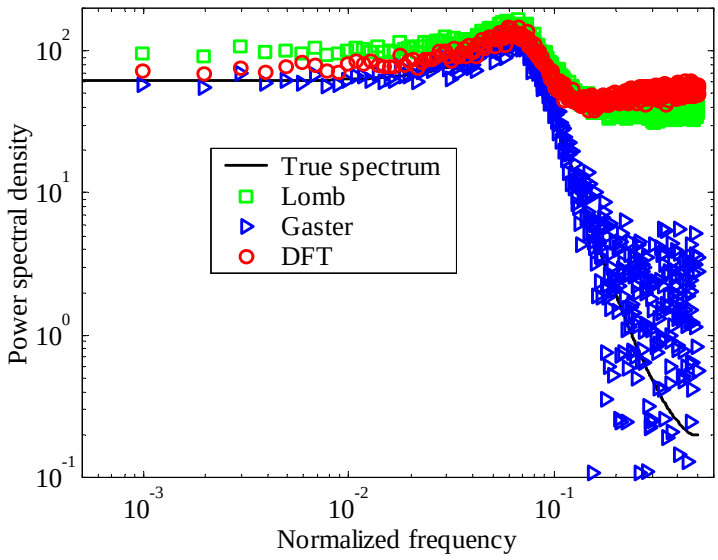

Figure 3.7: PSD estimates of a second order spectrum using Poisson distributed sample times (256 averages - mean frequency 50% of primary series)

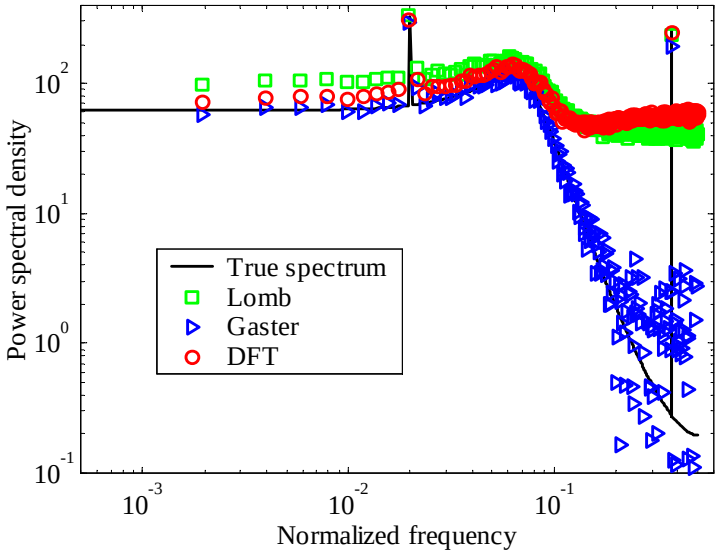

Figure 3.8: PSD estimates of a second order spectrum with two sine waves using Poisson distributed sample times (512 averages - mean frequency 50% of primary series)

set. A very interesting phenomenon is observed when white noise is added to the primary first order data series (no additional noise) after interpolation. The results are shown in Figure 3.10. All estimates except the Gaster estimate once again show the effect of the added noise. The Gaster estimate however follows without any effects of the added noise the original background first order spectrum. The only plausible explanation for this is that the Gaster estimate removes uncorrelated parts of the signal energy when estimating a PSD. Through the interpolation in Figure 3.9, the noise added to the data series has achieved some degree of correlation, whereas this is not the case when the noise is added after interpolation. It is beyond the scope of the work here to investigate this further but no mention of this effect has been found in the literature. This matter is very important for the interpretation of LDV measurements, where it is possible that bad data points make it into the final data set even past the elimination of low signal to noise ratio points. These bad data points, as they are likely random will not contribute to the energy of the power spectrum, if the power spectrum is estimated using the Gaster estimate (and the sample times are Poisson distributed).

The Gaster estimate appears quite powerful for the ideal Poisson time distribution. Figure 3.11 shows the results for a second order data set interpolated for a sample time distribution obtained from normalized actual LDV sample times. The figure shows that the Gaster estimate is still far superior to the other estimates. However, the estimate does show a noticeable offset from the true spectrum. An integration of the spectrum shows that in total, the Gaster estimate exceeds the true power of the signal by two percent. Adding white noise to the interpolated data set, similar to Figure 3.10 does not change the result for the Gaster estimate. The results are shown in Figure 3.12. The Gaster estimate exhibits the same amount of offset seen for the data set without added noise. The integration of the spectrum again yields an energy excess of two percent. The other estimators once again do capture the added white noise and are even further offset from the underlying second order spectrum.

These results show firmly that the best quality PSD estimate for LDV data

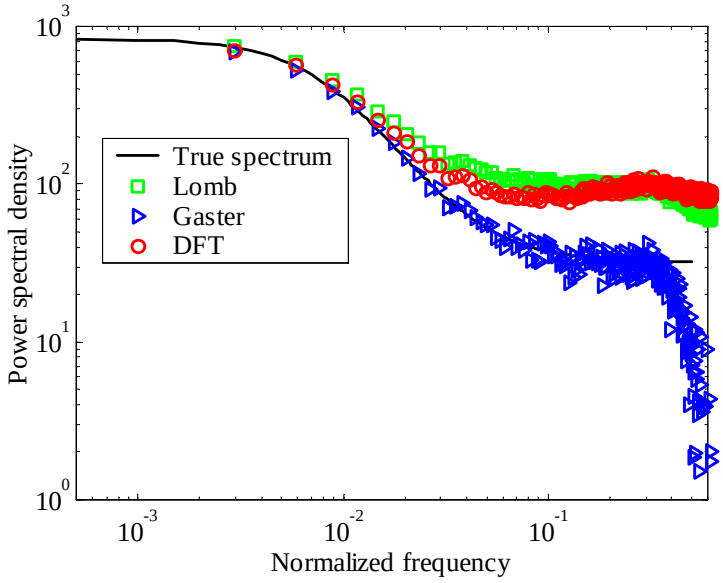

Figure 3.9: PSD estimates of a first order spectrum with white noise using Poisson distributed sample times (512 averages - mean frequency 75% of primary series)

is obtained from the Gaster estimate. All power spectra presented in the present study use the Gaster representation. Since the calculation for each frequency in the spectrum is independent of the next (in terms of algorithm), the range of frequencies calculated for true velocity data is divided up into double octaves. The frequency range is broken up at all points where the frequency has quadrupled. The block size used for averages at these frequencies is at least 128 samples long but the actual length is determined by the mean sampling frequency and the lowest frequency in the range. For a mean sampling frequency of 400 Hz, and a frequency range that begins with 1 Hz, the minimum block length required is 400 samples. The same power spectrum will however also be calculated at 200 Hz for which the minimum block length is 2 samples. In this case the 128 sample minimum block length is used. The power spectrum pieced together from these individual frequency averages will not have a constant variance. At low frequencies, the variance will be higher than at the high end of the frequency range. However, since most energy is contained at low frequencies, the increased variance may not be visible. At high frequencies, where the

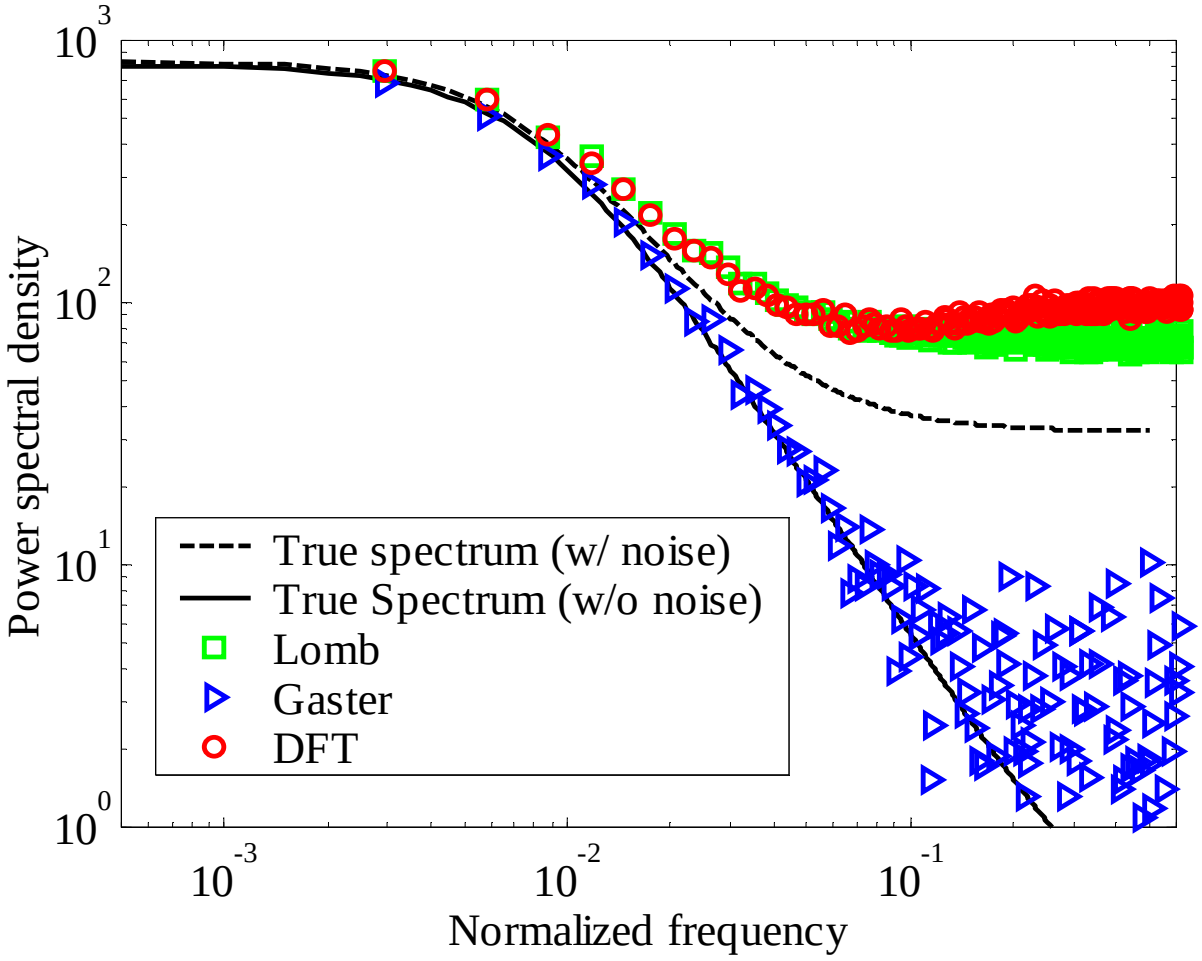

Figure 3.10: PSD estimates of a first order spectrum with white noise (added after interpolation) using Poisson distributed sample times (512 averages - mean frequency 75% of primary series)

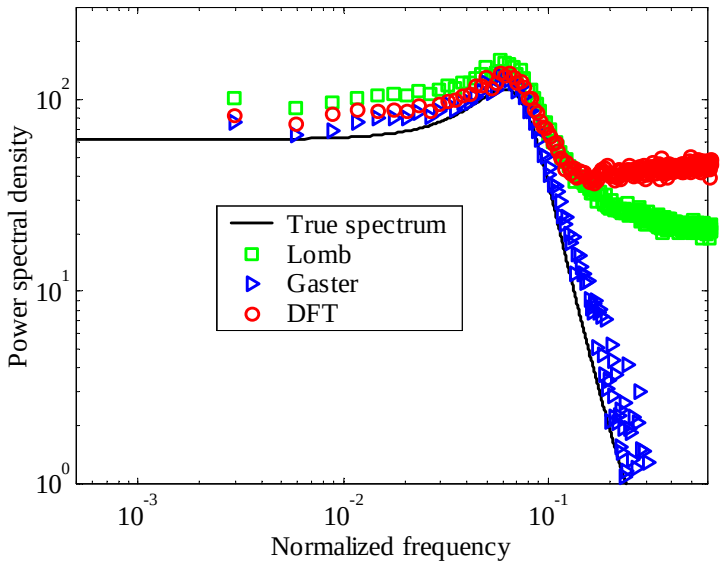

Figure 3.11: PSD estimates of a second order spectrum using a sample time distribution from measurements (512 averages - mean frequency 75% of primary series)

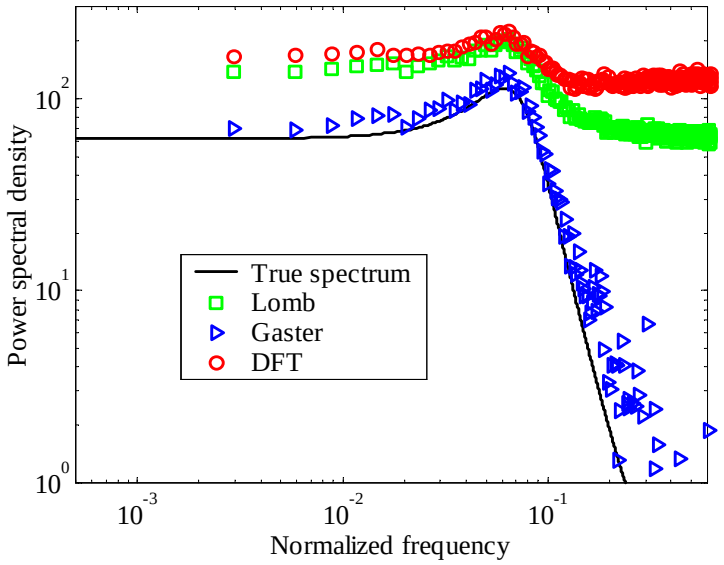

Figure 3.12: PSD estimates of a second order spectrum with added white noise (after interpolation) using a sample time distribution from measurements (512 averages - mean frequency 75% of primary series)

energy is low, the variance will be reduced and the spectrum will be visibly smoother.

The exact frequencies at which the spectrum is evaluated span the range from 1 Hz to 3/4 of the mean sampling frequency. The frequencies are spaced logarithmicly between 1 Hz and 2000 Hz. The upper limit of evaluation is either 2000 Hz or 3/4 of the mean sampling frequency, depending on which is lower. The frequencies at which the spectrum is calculated are not adjusted based on the mean sampling frequency of a data set. The result is that, in some cases, not all the power spectral density estimates are independent. This situation is analogous to zero-padding a data set in normal Fourier analysis. The result is an interpolation of the surrounding independent power spectral density points with some additional independent information added in. The additional information arises from the fact that the data was sampled randomly.

Cross-spectra can thus at this point not be calculated reliably using the DFT method except in cases where the mean sampling frequency is much higher than the frequency of interest. For some cases studied this is the case and results of cross-spectral analysis will be presented.

3.2.5 Measurement error

The error associated with the velocity measurements arises from mainly two sources. The first of the sources has to do with the alignment of the light beams inside the probe and the alignment of the probe with the experimental facility. The second source has to do with signal interpretation at the electronics and digital level. The errors will be discussed separately and then summarized quantitatively. The measurement error contribution is calculated using the commonly used root-square method for finding the combined effect of multiple uncertainties as given in Equation 3.14.

$$\begin{aligned} a1 &= g(b1, b2, b3, \ldots, N) \\ a1_{un} &= \sqrt{\sum_{i} = 1^{N} \left(\frac{\partial g}{\partial bi} u_{bi} \right)^2} \end{aligned} \tag{3.14}$$

3.2.5.1 Alignment

Measurement errors due to misalignment are further divided into two categories. The first deals with misalignment of probe optics that could cause an error in the fringe spacing. The second deals with the possible misalignment of the probe with respect to the experimental facility. The fringe spacing is a function of the light wavelength, beam diameter and focal length of the lens, as given in Equation 3.15.

$$d_f = \frac{\lambda\sqrt{d_b^2 + 4f_l^2}}{2d_b} \tag{3.15}$$

Using conservative estimates for the uncertainties in the beam separation and focal distance of the lens of three percent, Equation 3.14 can be used to find an overall uncertainty in the fringe spacing of 4.1%. Note that the resultant uncertainty is nearly equal to the uncertainty that would have been obtained, setting the partial derivatives equal to one (4.2%). Since the internal probe alignment does not change during a given test, deviations from the expected beam separation and focal distance cause a bias error in the velocity measurement. The error is present in every data point to the same degree.

The second source of alignment error is due to an angular misalignment of the probe with respect to experimental facility. This error is difficult to eliminate with the large facility used in the present study. In the measurements it is assumed that the LDV plane of measurement is aligned with the streamwise/cross–stream plane of the experimental facility. The misalignment between these planes about the three coordinate axes causes a bias error in the velocity measurement. Figure 3.13 shows a schematic that helps visualize the errors incurred. In addition, if the probe is aligned with the center of the test–section in the y-direction, then the y-component of velocity measured in a traverse along z will be the swirl (azimuthal) velocity component of the equivalent cylindrical coordinate system.

Angular misalignments between the probe and test section cause errors in the measurement of the desired components of velocity. Additionally some of these errors are a function of the other velocity components. Measurements of the swirl velocity

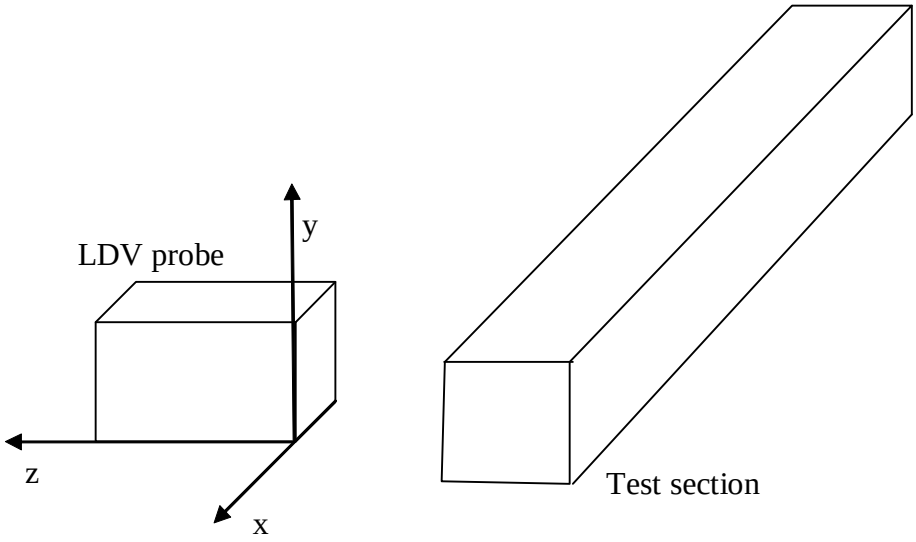

Figure 3.13: Alignment between test section and LDV probe

component are immune to a rotational misalignment about the y axis. Misalignment about the z-axis causes the swirl component to contain error directly proportional to the angle and the axial velocity. Misalignment about the x-axis causes the swirl component to contain error directly proportional to the angle and the radial velocity. The axial velocity component is immune to misalignment about the x axis. Misalignment about the y-axis causes an error in the measured axial velocity component proportional to the angle and the radial velocity. Misalignment about the z-axis causes an error proportional to the angle and the swirl velocity. Additionally, all misalignments cause an error in the location of the probe.

Using a level, the test section and probe could be aligned to each other with respect to the z- and x-axes to within two degrees. Rotational misalignment about the z-axis would become evident through changes in the location of the zero-crossing of the swirl velocity as the axial velocity component develops and changes in the downstream direction. The measurements did not exhibit a clear drift in the vortex core location. If all velocity components are nearly equal then a two degree rotational misalignment causes about a three percent error in the measured velocity. These

errors can be much larger in areas where the desired velocity component is small as with for example the swirl velocity component near the vortex core.

In addition to the errors associated with rotational misalignment, a translational misalignment between the test section radial line and the experimental z-axis traverse will introduce additional errors inversely proportional to the radial coordinate of measurement. The desired swirl component of velocity is most susceptible to this type of misalignment. However, the collocation of the z-axis traverse with the radial line was able to be precisely estimated from scans of the axial velocity profile in the y-direction inside the nozzle, knowing that the maximum of axial velocity at each z location will occur when the radial line is parallel to (crosses) the z axis.

The errors due to rotational probe misalignment are difficult to quantify and will contaminate the data with both bias and random components due to the error's dependence on instantaneous velocity. Experiments did not show clear evidence of misalignment. Nevertheless it is estimated that rotational alignment errors contribute around three percent uncertainty to the measurement.

3.2.6 Frequency estimation error

The error in the estimation of the Doppler frequency is composed of the error in the original shift frequency, the error in the mixing frequency and the error in the estimation of the burst frequency. The original shift frequency is equal to 40 MHz with a very small uncertainty of 0.001 MHz. The mixing frequency is measured to within 0.001 MHz but can drift slightly over the period measurements are taken. The drift is in general less than 0.01 MHz. The error in the estimation of the burst frequency is difficult to quantify. From Figure A.33 and Figure A.34 it can be seen that the two methods of frequency identification compared in these figures have differences only inside the five percent deviation window. A conservative estimate for the error due to burst frequency estimation is thus five percent. Since the Doppler frequency is a simple sum and difference of the mentioned frequency components, it is clear that the error in the Doppler frequency estimate is dominated by the burst frequency estimation error. It was not possible to determine whether or not the estimation error

is entirely random, but the figures cited above seem to lend support to the idea that the errors are at least best described as random.

3.2.7 Total velocity uncertainty

The total uncertainty for velocity measurements can now be estimated. Since all three error sources discussed are independent, the sum-square method is once again used to determine the total uncertainty. The uncertainty in the Doppler frequency estimation and the fringe spacing combine to result in a 6.4% uncertainty. Since there is no straightforward equation relating the measured velocity to the probe alignment error, these errors will be combined assuming equal contributions (partial derivatives equal to one). The resulting uncertainty has a magnitude of 8%. This uncertainty contains both the contributions of random and bias error. Accounting only for errors that change from data point to data point, the uncertainty is equal to 7%. Error bars will not be plotted in the data reported in order to clarify the presentation. The similarity of measurements at different flow rates reported in Chapter 4 shows that the repeatability of the measurements is very good and well below 7 %.

3.3 Acoustic measurements

Acoustic measurements were performed to help characterize the dynamic flow field and help describe interaction between the flow field and the acoustic field. The microphones used in the present study are constructed from condenser microphone cartridges by Panasonic in a aluminum threaded rod package. Both resistor and capacitor components are inside the machined aluminum threaded rod. Cost for each microphone, excluding the minor machining of the aluminum threaded rod, is around five dollars. BNC connectors are provided for the microphone signal and excitation voltage. A photograph of a microphone is shown in Figure 3.14.

Figure 3.14: Custom microphone package

3.3.1 Calibration

A detailed description of the microphone sensor calibration is given in Appendix B. All microphones were calibrated against a Bruel&Kjaer reference inside a long closed–driven tube. To ensure that each microphone is exposed to the identical acoustic pressure, the microphones were located flush with the end wall of the tube. The frequency calibration range for the present experiments is 0-200 Hz. Microphone response is essentially flat starting at 20 Hz. The microphone cartridges are designed for use in the frequency range of 20 to 20,000 Hz.

3.3.2 Acoustic velocity and intensity

As briefly mentioned in Chapter 1, the interaction between the essentially incompressible low Mach number flow field and the acoustic field is an important component of the present research. The interaction can be separated into two main mechanisms. The first mechanism of interaction is through acoustic velocity. The second mechanism of interaction is through the dissipation of acoustic energy and conversion to vorticity.

The velocity perturbations associated with an acoustic wave are proportional to the local pressure gradient. For plane waves, at low Mach numbers, the acoustic

velocity field is related to the acoustic pressure field through Equation 3.16 which is derived from the Euler equation (Crocker and Waser, 1984). Exciting the pressure field with a speaker causes a distributed excitation of the flow field from the acoustic velocity oscillations. An important consequence is that the phase between velocity oscillations at different axial locations is related through the speed of the acoustic pressure wave which is much higher than the speed of incompressible velocity instability waves. The speed of incompressible velocity instability waves is on the order of the mean flow velocity, so that there exists a complete mismatch of time scales for low Mach number flows between incompressible velocity instability waves and acoustic velocity waves.

$$\frac{\partial \vec{u}}{\partial t} = -\frac{1}{\rho}\nabla p \tag{3.16}$$

The mismatch of time scales between incompressible instability waves and acoustic velocity waves leads to the hypothesis that another mechanism must be responsible for the ability of a flow instability to lock on to acoustic excitation. The proposed mechanism is that of localized dissipation of acoustic energy and conversion to vortical energy. Conversion of acoustic energy into vorticity occurs only at sharp boundaries where shear layer separation occurs. The thin shear layer shed in the immediate vicinity of a sharp interface allows a local match between the acoustic and incompressible time scales. The dissipation of acoustic energy is especially pronounced at low frequencies (Bechert et al., 1977). Munt (1990) shows that in order to successfully model the dissipation, a Kutta condition must be imposed on the flow at the sharp interface. The measurement of acoustic intensity in the test facility upstream and downstream of the area expansion (the sharp interface in this case) may allow some conclusions to be drawn with respect to the amount of acoustic dissipation at the area expansion. Acoustic intensity is the local acoustic energy density. Local measurements cannot measure total acoustic energy dissipation without the assumption of plane wave acoustics. The validity of these assumptions and the results will be discussed further in Chapter 5.

Acoustic intensity is calculated from two acoustic pressure measurements using

either the method of Crocker and Waser (1984) or the method of Chung and Blaser (1980). Crocker and Waser (1984) offer a direct way of calculating acoustic intensity via the measurement of the cross-spectrum between two microphones. Chung and Blaser (1980) propose a transfer function method for the determination of the transmission properties of an acoustic termination. A method for improving the transmission property estimate through the use of a third microphone in high background noise environments is also given. The acoustic intensity as a function of the one-sided cross spectrum between microphones one and two is given in Equation 3.17 (Crocker and Waser, 1984).

$$I(\omega) = -\frac{Im\left(P_1^* P_2\right)}{2\omega\rho\Delta r} \tag{3.17}$$

The reflection coefficient of an acoustic termination or obstruction is given by Equation 3.18 (Chung and Blaser, 1980). The reflection coefficient given here is a complex quantity that is a function of the physical location of microphone 1 with respect to the acoustic obstruction. The absolute value of the reflection coefficient figures into the calculation of the transmitted power. The expression for the power transmitted through the acoustic obstruction as a function of the pressure magnitude at microphone location 1 and the reflection coefficient is given in Equation 3.19.

$$R_p = \frac{H_{12} - e^{ik_i\Delta r}}{e^{-ik_r\Delta r} - H_{12}} \tag{3.18}$$

$$W_T = \frac{A}{\rho c}|P_1|^2\frac{1 - |R_p|^2}{|1 + R_p|^2} \tag{3.19}$$

The measured transfer function can be corrected to obtain a better estimate using a third microphone. The equation for the corrected transfer function, is given in Equation 3.20 in terms of the calibration and acquisition corrected measured transfer function, H_{12}^m. The correction depends on the ordinary coherence functions between the three microphones used in the measurement. The coefficients in the equation actually consist of the positive square root of the ordinary coherence function in question. The equation for a generic coefficient is given in Equation 3.21.

$$H_{12} = H_{12}^{m} \frac{c_{23}}{(c_{12}c_{31})} \tag{3.20}$$

$$c_{jk} = \sqrt{\frac{|P_j^* P_k|^2}{(P_j P_j^*)(P_k P_k*)}} \tag{3.21}$$

All data acquisition clearly initially has units of volts and these units must be converted to pressure, using the measured calibration transfer functions. Additionally, the measurements performed using the PC data acquisition system are subject to an inter-channel delay because the card used in these measurements does not have the simultaneous sample and hold feature. The inter-channel delay was set to 5 μsec and verified by measuring sine waves of various frequencies on all channels at the same time. Equation 3.22 shows how the measured transfer function between two microphones is corrected using the calibration and channel delay adjustments necessary. The calculation of the actual pressure magnitude from the measured voltage magnitude is given in Equation 3.23. The calculation of the actual cross spectrum from the measured voltage cross spectrum between two microphones is given in Equation 3.24.

$$H_{12}^{m} = H_{12}^{v} \frac{Cal_1}{Cal_2} e^{-i\omega(ch_2 - ch_1)ch_d} \tag{3.22}$$

$$|P_1| = \frac{|P_1^v|}{|Cal_1|} \tag{3.23}$$

$$(P_1^* P_2) = \frac{((P_1^v)^* P_2^v)}{Cal_1^* Cal_2} e^{-i\omega(ch_2 - ch_1)ch_d} \tag{3.24}$$